Graphene nanomesh photodetector with effective charge tunnelling from quantum dots†

Xiang Liu,‡[a] Nianze Liu,‡[a] Mingju Liu,[b] Zhi Tao,[a] Wenjian Kuang,[a] Xiangbing Ji,[a] Jing Chen,[a] Wei Lei,*[c] Qing Dai,*[b] Chi Li,*[b] Xuehua Li[a] and Arokia Nathan[b]

Graphene nanomesh (GNM)-based optoelectronics integrated with quantum dots (QDs) are investigated in this article. The charge transfer mechanism in the QDs/GNM interface is probed in four terminal gated FET-type photodetectors. The insulating ligand is used to make the GNM/ligand/QDs vertically behave like a metal/insulate/semiconductor (MIS) structure to facilitate the charge tunnelling. With the current constraint effect of the GNM and the effective charge tunnelling, a high-performance photodetector is fabricated with higher responsivity, higher on/off ratio and shorter response time. The results of our analysis and experimental approach can be extended to future graphene-based photodetectors, as long as suitable ligands and an effective architecture are chosen for this type of device.

1. Introduction

Graphene-based photodetectors, as highly desired devices for various applications from telecommunication, biological imaging to remote sensing,[1–4] are atomic layer two-dimensional (2D) materials possessing unprecedented electric and optical properties.[5–7] Especially, based on the research on the graphene-based photodetector, many recent studies have concentrated on increasing the responsivity, response (measured) time and operation wavelength. To overcome the low responsivity[8,9] of pristine graphene (<0.1 A W^{-1}) under illumination of the incident light, ingenious device structures have been proposed in previously reported papers. These include field effective transistor (FET) device with graphene-quantum dots (QDs) hybrid channel, which gives higher responsivity but sacrifices the measurement speed;[10] waveguide graphene photodetectors with special micro-nanostructure, which accelerate the response speed with a relatively high responsivity over 0.1 A W^{-1};[11,12] reduced graphene oxide phototransistors featuring defect and atomic structure control, which outperform pristine graphene devices in terms of photoresponses at the cost of response rate;[8] and some other devices such as those with metallic or graphene plasmonic[13–15] micro-nanostructure, which have also immensely attracted the interest of researchers all over the world.

However, regardless of which photo-sensing architectures are chosen to compose the photodetectors, the dynamic charge transfer or energy transfer between the graphene and active components (such as QDs, silicon)[16,17] would always occur in the photo-sensing region. If one looks at the graphene-QDs hybrid material system, many problems in the interface between graphene and QDs emerge because the excited QDs need to transfer the electrons or holes to the graphene. To solve these problems in graphene photodetectors, many research groups around the world have utilized the specific structure of gated graphene FET transistors to manipulate the charge transfer between graphene and QDs driven by the gate bias, and have achieved high photosensitivity, high responsivity and broad response waveband.[18]

Due to the offset work function between graphene and QDs material, the Schottky barrier between QDs and graphene can hinder the direct charge transport from QDs to graphene. In fact, without the bonding of the ligand in QDs surface, the QDs cannot be steadily decorated on the graphene interface.[19] Nevertheless, recent reported papers on this type of photodetectors have ignored this factor or have simply just chosen an electroactive ligand without evaluating the charge transfer efficiency or mechanism in this process. Thus, different charge transfer mechanisms have been deeply explored in this paper to optimize the fabrication process, material selection and operation performance of the graphene-QDs hybrid photodetectors.

[a]*Electronic Science and Engineering School, Southeast University, Nanjing, China. E-mail: lw@seu.edu.cn*

[b]*National Center for Nanoscience & Technology, Beijing, China. E-mail: daiq@nanoctr.cn, lichi@nanoctr.cn*

[c]*London Center for Nanotechnology, University College London, London WC1H 0AH, UK*

†Electronic supplementary information (ESI) available: The TEM image of all the four QDs with different ligands, the PL and UV-vis spectra of QDs and the GNM/QDs with different ligands and the testing device on the probe station under the LED light. See DOI: 10.1039/c4nr06883a

‡Xiang Liu and Nianze Liu are contributed equally to this work.

The absence of bandgap in graphene is another dampener, due to which the dark current is so high and the on/off ratio[20] (about 1–3) is so low that even the noise photocurrent occurring in the test will considerably interfere with the experimental result. As a result, it is difficult to contrast the charge transfer efficiency differences between the QDs with various ligands. Consequently, a nanomesh structure was employed in the graphene to open the bandgap and constrain the dark (leakage) current.[21]

Finally, in this work, the excited charges induced by incident light in n-type semiconductor CdSe QDs effectively tunnels through insulating ligand (it is thought to be ineffective for charge transfer in many previous papers) to the graphene nanomesh (GNM) channel, which behaves like a MIS (metal-insulate-semiconductor)[22,23] structure vertically due to the enhanced electric field intensity caused by the bottom gate voltage. It is worth believing that it will contribute immensely toward the future applications of the graphene-based photodetectors with the optimization of the charge transfer efficiency in channel of the FET-type photodetectors.

2. Results and discussion

2.1 Characterization of the GNM FET device

2.1.1 Schematic of the GNM FET device fabrication process and the morphology of the GNM channel. The abbreviated cross-sectional fabrication process flow is depicted in Fig. 1a, which describes the two main steps: the formation of the GNM, and then the bonding between GNM and QDs with different ligands. The width of the graphene nanoribbon in GNM is approximately 20 nm (GNM can be treated as graphene nanoribbon networks, which is shown in Fig. 1c) using aluminium-anode-oxide (AAO) membrane mask (shown in Fig. 1a and b). To investigate the formed GNM, Raman spectra measurement (Fig. 1e) was carried out to ensure that, compared with the pristine graphene, the GNM in our work was a typical p-type graphene,[20,24,25] resulting from the ambient oxidation of the graphene nanoribbon and the influence of the etching process. In addition, Fig. 1d illustrates the 20/200 μm channel (1 : 10 *W*/*L* ratio) of the FET device and inset image shows the morphology of the QDs (4.8 nm diameter, 590 nm peak emission shown in Fig. 2c and Fig. S1†) decorated GNM in the FET channel. In addition, the encapsulated ligand outside the QDs is unstable without any treatment, which will cause the decrease in the photo-absorption and charge transfer capability. Thus, the approximately 25 nm thick QDs layer was bonded on the channel through an annealed process, which can be illustrated in the AFM image of Fig. 2d. Herein, the annealing process is essential to form a stable ligand layer with a colloidal morphology, which can benefit the formation of the coordination bond between GNM and conjugated organic shell of QDs. The typical annealed effect toward TOPO ligand is also investigated in Fig. S4a.†

2.1.2 Transfer characteristic curve of the pristine graphene/graphene-QDs hybrid and pristine GNM/GNM-QDs hybrids. The effects of the GNM channel and deposition of QDs on the FET's transfer character are shown in Fig. 1f. First, herein, the p-type semiconductor behaviour can be observed, which agrees with the previous investigation with the Raman

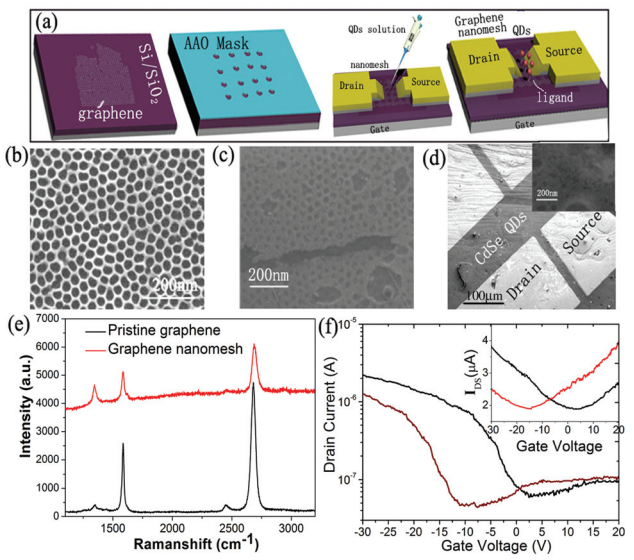

Fig. 1 Characterization of the GNM/QDs photodetectors. (a) Cross-sectional abbreviated fabrication process flow of the GNM/QDs photodetectors. (b) SEM image of the AAO mask. (c) GNM morphology after the etching treatment and removal of the AAO mask. (d) A SEM image of the FET device channel and the QDs decorated GNM. (e) The Raman spectrum of pristine graphene and GNM. (f) Transfer characteristic curve of GNM and GNM/QDs(TOPO) FET and that of pristine graphene FET(inset) for V_{DS} = 30 mV.

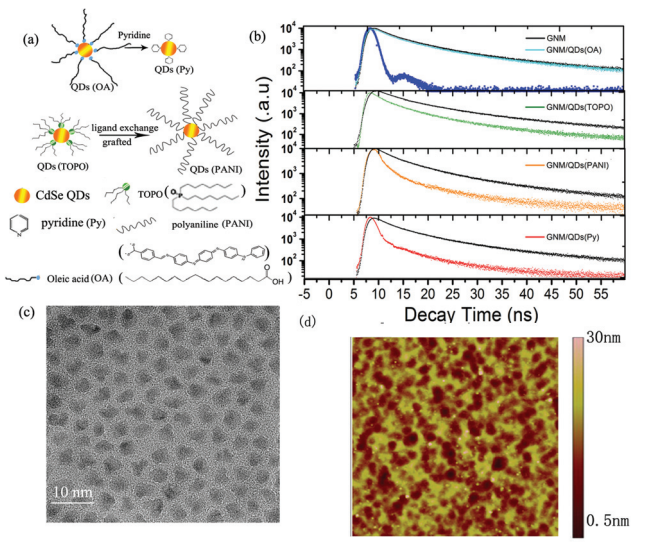

Fig. 2 (a) Molecular structures of as-prepared QDs capped with four different ligands and the schematic diagram of the ligand exchange from QDs (TOPO) to QDs capped with electroactive ligands (QDs (Py) and QDs (PANI)). (b) Time-resolved PL decay spectra for pristine GNM interface blended with QDs(OA), QDs(TOPO), QDs(PANI), QDs(Py). (c) The TEM image of well-dispersed QDs(OA) solution. (d) The AFM image of deposited QDs films bonded to graphene channel after annealing.

spectrum.[26] Second, according to reported papers,[27] the bandgap of 2D graphene is predicted to even reach 200 meV under some certain ambient conditions through the constraints of the narrow graphene nanoribbon, which will exhibit a higher on/off ratio. As depicted in Fig. 1f, the on/off ratio of the as-fabricated FET photodetector is about 30 in our work. In addition, the on/off current ratio, another trend of the Dirac point blue shift is also demonstrated in the Fig. 1f, which is induced by the deposition of the QDs. The doping of the n-type semiconductor CdSe QDs (which has a 4.2–4.3 eV work function) is the predominant n-doping in the GNM channel because the work function of graphene is about 4.6 eV.

2.2 Photoelectric trigger characteristics of the GNM photodetectors

2.2.1 Photoluminescent (PL) decay measurement and mechanism of the charge transfer without bottom gate voltage. The electron transfer between QDs and graphene through the ligand can be monitored by utilizing transient PL decay spectroscopy. Under 444 nm incident laser, the four QDs@ligand samples (as shown in Fig. 2c and Fig. S1 a–c†) on the GNM silica substrate (Fig. 2d) were bonded onto the detection to measure the lifetime variation, which can be used to probe the PL quenching effect.

According to the steady-state PL decay spectra in Fig. 2b, QDs capped with electroactive ligands showed a stronger PL quenching substantiation compared with the QDs capped with insulating ligands. With less defects, shorter molecular structure (Fig. 2a) and better electric conductivity, it seems plausible that only electroactive ligands such as pyridine and PANI can facilitate the charge transport from QDs to graphene in the graphene/QDs hybrid system, attesting to the similar results reported in previous papers.[19,28–31] Insulating ligands (such as OA), on the other hand, have no ability to efficiently transfer the charge carrier.[10,19] Any weak charge transfer from QDs within insulating ligands (in case of TOPO and OA) may simply be caused by a weak built-in field in the excited-QDs/graphene hybrid interface that cannot supply the ligand a sufficient tunnelling ability due to the lack of external gate bias. However, it is likely that, when the gate bias is large enough to enable a considerable tunnelling process, insulating ligands may also be able to considerably facilitate the charge transfer.

To better illustrate the hypothesis *ab initio*, the electric field intensity (E, V nm^{-1}) distribution of the nanostructure device was simulated by the finite element method (FEM) using COMSOL Multiphysics (v. 3.5a). As shown in Fig. 3a and b, with the gate bias set from 5 V, 10 V, 15 V to 20 V, the electric field intensity distribution was calculated to predict the GNM/QDs device operation. In the case of small gate voltage (5 V and 10 V) or non-gate voltage under illumination, the electric field density in the insulating ligand device is similar to that in the electroactive ligand device. Nevertheless, the uniform electric field intensity distribution in the electroactive ligand will benefit the charge transport from QDs, as proved in above PL decay spectra results. However, with the increase of gate

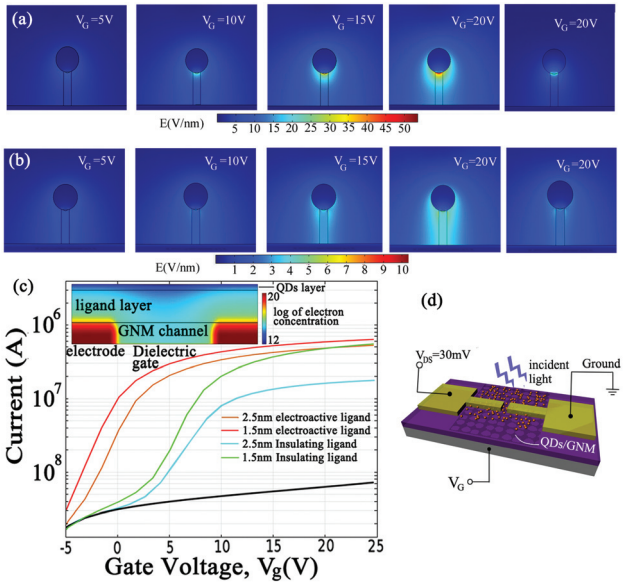

Fig. 3 Simulated enhanced built-in electric field in GNM/electroactive-ligands/QDs (a) and MIS structure of insulating ligands (b) for (left to right) V_g = 5 V, 10 V, 15 V, 20 V and in darkness(20 V). (c) The simulated transfer I_D–V_g curve of the GNM/ligand/QDs FET device for V_{DS} = 5 mV and the log distribution image of electron concentration (inset). (d) The schematic image of the GNM/QD FET photodetector testing circuit.

bias to 15 V and 20 V (maybe exceeding the threshold tunnelling voltage), large amount of excited electrons accumulate on the interface of QDs, producing an enhanced electric field intensity within this QDs/ligands/graphene system, and leading to the increase in tunnelling rate. On the other side, the electric field intensity of the electroactive ligand device only grows slightly compared with the largely enhanced electric field intensity of the insulating ligand device. Here comes the question: is it a convincing conclusion that GNM/QDs device with the insulating ligand is also a desirable candidate for the gated FET-type photodetector in practice?

Alternatively, the simulation model of GNM with punched periodic nanoholes has been investigated and demonstrated with the nearest-neighbor tight-binding (TB) Hamiltonian method to define and describe the graphene lattice.[21] To focus the study on the charge transfer and the influence of the gated FET structure, the p-doped GNM channel was modelled as the p-type semiconductor component with ideal 200 meV bandgap (and other GNM property parameters), which operates like a conventional FET device using quasi-fermi levels in classical regime. The discrete QDs/ligand layer in reality, was treated as continuous layer for calculation, as shown in the inset image of Fig. 3c, in which the ligand component was configured as either electroactive or with insulating properties. In this electron concentration distribution image, the excited electron accumulating on the n-type-QDs/ligand interface can be driven to the p-type GNM channel by the built-in voltage (caused by FET's gate bias), which, at the same time, traps the holes within the QDs. It is worth noting that, in the case of insulating ligand, the device vertically was configured as a p–i–n

structure, in which the tunnelling efficiency is determined by the ligand length due to the same parameters (such as relative permittivity ε_r and trap state density N_t) defined in our simulation work. The simulated transfer current curve suggests that rapid current growth (green and blue curves in Fig. 3c) can be obtained in an insulating ligand device when the gate voltage exceeds the threshold voltage and that its current reaches almost the same saturation current with the electroactive counterparts. Thus, to verify the efficiency of charge transfer in practical gated FET-type photodetectors with different ligands, a series of experiments on the photoelectric properties were then carried out.

2.2.2 Photoelectric property of the GNM/QDs FET photodetector. The photoelectric property testing loop is shown in Fig. 3d, to probe the photocurrent of the device under incident light and different gate voltage (V_G). The experimental result in Fig. 4a with the transfer characteristic comparison shows the Dirac point shift of the different four devices under darkness. The electroactive ligand (Py and PANI) more effectively transferred the electrons to the GNM to cause a larger Dirac point shift and dark (leakage) current, in agreement with the simulated results under darkness as described earlier.

Fig. 4c and d contrast the photocurrent gain of the GNM/QDs devices with different ligands on the same incident light wavelength and luminous density (λ = 400 nm, ρ = 17 μW cm^{-2}). The obvious higher dark/light current ratio can be demonstrated in this experiment as a result of the GNM's current constraint effect. Owing to this effect, even the photocurrent of the GNM/QDs(OA) device can be observed, whereas in the case of pristine graphene/QDs(OA) device, little of the phenomenon occurs according to previously reported results.[10,19] Interestingly, the GNM/QDs(TOPO) device has almost the same saturated photocurrent compared with the GNM/QDs(Py) device and is about fourfold than that of GNM/QDs(PANI) when added to the positive gate voltage. It is also worthwhile to note that the photocurrent of these four devices agree with the results of the previous PL decay spectra at V_G = 0 V, as shown in Fig. 4c and d. In addition, the rapidly increased voltage-sensitive photocurrent of the GNM/QDs (TOPO) device accompanied by the increasing gate voltage can be viewed in Fig. 4c, and the threshold tunnelling voltage of this device is estimated to be about 2 V, as suggested from our simulated work.

By referring to the energy level alignment diagram[19,32–34] in Fig. 4b, it is clear that, while the low LUMO (lowest unoccupied molecular orbital) electroactive ligands (pyridine and PANI) can transfer the electrons feasibly, the high LUMO electroinertia insulating ligands (OA and TOPO) can only drive electrons by directly tunneling from the semiconducting QDs to graphene. Within this framework, the tunnelling barrier can be effectively reduced by increasing gate voltage. Therefore, by studying the experimental data and simulated results, it can be believed to be arbitrary to claim that electroinertia insulating ligands cannot be used in this hybrid FET photodetector.

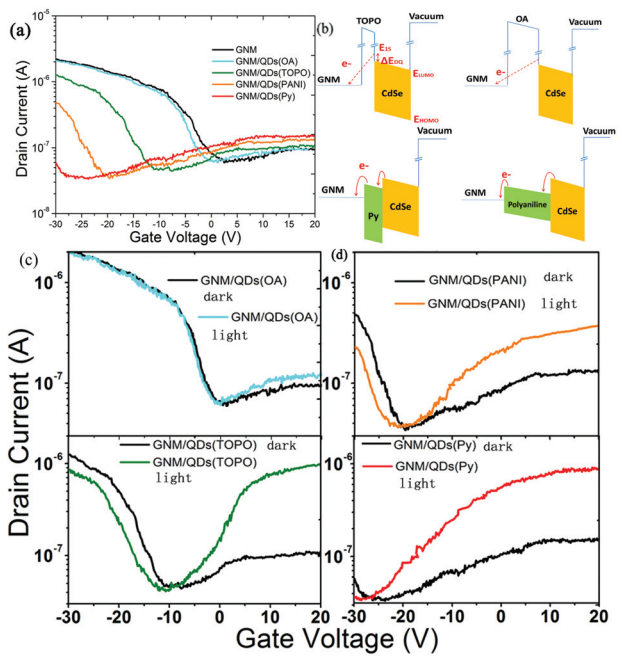

Fig. 4 (a) Electric properties measurement of the GNM/QDs FET photodetector without illumination (V_{ds} = 30 mV). (b) Band alignment diagram of the charger transfer of QDs/ligand/GNM structure. (c) and (d): Transfer character test of the four different samples under the incident 400 nm light at 17 μW cm^{-2} luminous density, and 30 mV Drain–Source voltage (V_D).

2.3 Charge tunnelling and transport mechanism and device performance characterization.

2.3.1 Electron transfer efficiency mechanism. The photocurrent of the GNM/QDs(TOPO) device is still 1–2 orders of magnitude higher than that of the GNM/QDs(OA) device (though they all belong to insulating ligands), and the simulated current difference between the 1.5 nm and 2.5 nm ligand layer (green and blue curve in Fig. 3c) is much smaller than the experiment result. Hence, it is essential to explore the determinant factors for facilitating an effective charge transfer. One obvious reason is that the field intensity (E (V nm^{-1})) in the shorter ligands TOPO (~1.5 nm) and pyridine (~0.5 nm) is larger than their longer counterparts OA (~2.5 nm) and PANI (>2.5 nm), which will promote the dynamic charge transfer. However, it cannot explain the photocurrent magnitude difference between TOPO and OA, and the only 2 or 3 times photocurrent difference between pyridine and PANI.

In case of tunnelling mechanism (TOPO and OA wrapped devices), because the electron on E_{LUMO} (the bottom of conduction band) of QDs has a zero wave vector (k-vector), the tunnelling electron that manages to escape from the QDs should at least be at the 1S-state of QDs ($E_{1S} = E_{LUMO} + \Delta E_{QD}$) such that there is enough energy to tunnel through the potential barrier (as shown in the energy level diagram of GNM/QDs (TOPO) in Fig. 4b). In order to estimate the escape time for 1S-state electrons of QD, the tunnelling rate K_{tun} is reported[35] to have been applied in a semi-classical approximation as

$$K_{tun} = A f_{QDs} P_{tun}, \quad (1)$$

where A, f_{QDs}, P_{tun} is the empirical constant standing for the effective tunnelling area in the surface of QD, electron semi-classical oscillation frequency and quasi-classical probability of tunnelling, respectively.

Among them, f_{QDs}, P_{tun} can be calculated as:

$$f_{QDs} = v_e/2d_{QDs},\ v_e = \sqrt{\frac{2E_{1S}}{m_{eff}}} \quad (2)$$

$$P_{tun} = e^{-\frac{2}{\hbar}\int_0^{L_{lig}} dz|p(z)|},\ p(z) = \sqrt{2m_{eff}(z)(E_{1S} - U(z))} \quad (3)$$

where, v_e is the characteristic electron velocity, while electron is in the 1S-state, d_{QD} is the QDs diameter, m_{eff} is the effective mass of the electron, $\hbar$ is plank constant, the integral is taken over the tunnel path (L_{lig}, ligand length) going through the potential barrier, $U(z)$ is the electron potential along the tunneling path and $m_{eff}(z)$ is the effective mass of the electron taken along the tunneling path.

This simple model can be used to correlate with the results observed in our experiment. When the length of QDs' encapsulation ligand is increased from TOPO(~1.2 nm) to OA (~2.5 nm), L_{lig} is increased more than twofold, resulting in rapid weakening of probability of tunnelling P_{tun} due to the exponential relationship between P_{tun} and the L_{lig}'s integral. In addition to ligand length, because the effective tunnelling barrier is another impact factor as shown in the formula of $p(z)$, the TOPO ligand with advantage of a lower E_{LUMO} ($U(z) = E_{LUMO}$) also curtails the effective tunnelling barrier. After the gate voltage reaches a threshold value, the photocurrent of the GNM/QDs device will tremendously increase due to the rapidly decreased tunnelling barrier, which is described in the experiment of Fig. 4c. As for the OA ligand, which is considered as a more insulating material, it causes a much lower probability of tunnelling P_{tun} due to the exponential nature of these parameters ($p(z)$ and P_{tun}). In our experiment, because the photocurrent of OA device was maintained at a limited level in Fig. 4c, we suppose that the threshold voltage of OA is too high to reach, resulting from the long ligand length and the higher tunnelling barrier (high LUMO). Thus, in addition to the length difference, the additional tunnelling barrier difference for excited electrons along the tunnelling path of TOPO and OA makes it difficult to configure all the parameters in our simulated model as the real situation, which explains the relatively large discrepancy between the simulated curve in Fig. 3c and experiment curve in Fig. 4c:

As for another charge transport mechanism in pyridine and PANI wrapped device, the ligands in these devices operate like an electron transport layer.[19] Thus, we ruled out the impact of electron tunnelling between QDs and GNM: the influencing factors here should be the field intensity (E (V nm^{-1})), the conductivity and the defects in these materials, as predicted and configured in the simulated work. Considering the stronger field intensity, better conductivity and less defects (due to the shorter length and easy ligand exchange process), it is not difficult to understand why the photocurrent of GNM/QDs(Py) is 2–3 times higher than that of GNM/QDs(PANI), and the result that the simulated transfer character curve of different ligand length shows the similar trend as the experiment data.

2.3.2 Device response performance characterization. Fig. 5a depicts the sensitive stable on/off photocurrent (GNM/QDs (TOPO)) of I_D at different gates voltage toward the illumination. Due to free photoinduced electrons transferred from excited QDs to GNM driven by built-in voltage and drifted by the drain–source voltage (V_D), a significant photocurrent increase in GNM/QDs hybrid is found at +4 V V_G, where graphene is an n-type semiconductor. On the flip side decrease in photocurrent is obtained at −24 V, where hole carriers would be scattered in p-type graphene and the recombination with extra electrons from the excited n-type QDs diminishes the hole carrier density in GNM channel.[31]

High response capability under high speed testing conditions is another pivotal performance index of the photodetectors. As a consequence, the time-dependent response current to the pulse light signal was probed and the comparison result toward different ligands is shown in Fig. 5b. The detailed time trace response probed voltage variation of TOPO-wrapped and OA-wrapped devices measured by different load resistance (2.5 kΩfor TOPO, 20 kΩ for OA) and high frequency oscilloscope is shown in Fig. S3b.† In these dynamic response experiments, the V_D and V_G are fixed at 30 mV and 15 V, respectively. The on-state photocurrent rise time can be estimated to be about 50 ms, 15 ms, >1 s and 0.75 s for OA, TOPO, PANI and pyridine wrapped QDs/GNM devices, respectively, from the pulse response signal in Fig. 5b and c. A shorter response time in electron tunnelling ligands device was

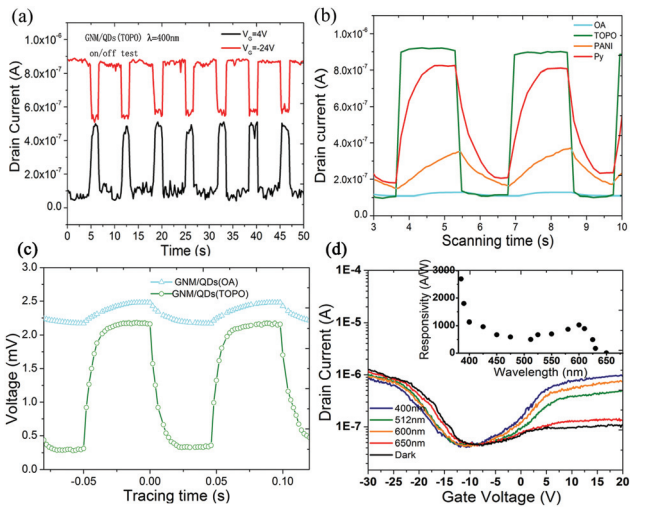

Fig. 5 (a) On/off photoelectric properties of the GNM/QDs(TOPO) photodetector at +4 V and −24 V. (b) The photocurrent on/off response time comparison of the four GNM/QDs devices with different ligands (under 17 μW cm^{-2}, 400 nm incident light, V_{DS} = 30 mV). (c) Voltage variation on load resistance in response to on/off illumination experiment in electron tunnelling ligands device (TOPO and OA) for V_{DS} = 30 mV. (d) The transfer characteristic curve of the GNM/QDs(TOPO) device was measured under 17 μW cm^{-2} luminous density by different wavelengths and the calculated responsivity of this device (inset) at V_G = 15 V and V_{DS} = 30 mV.

observed in the time-dependence experiment. After turning on the light, the free excited electrons in QDs will directly tunnel to the GNM without staying in the ligands, while in the transport mechanism device, many defects and impurities in the ligands will capture the transport electrons and extend the electron exchange time. However, obviously, compared with nanosecond level QDs quenching time, millisecond device response time is much longer. This phenomenon possibly comes from the excited electron accumulation time in the QD/ligand interface, which will reach a built-in threshold voltage to facilitate the charge tunnelling. It is obvious that the shorter ligand (TOPO) has a much lower threshold voltage for the electron tunnelling.[36] On the other hand, the ligand length should be a very important constant for the electroactive ligands of the devices in dynamic response photocurrent. The electron charge transfer process in vertical structure can be equivalent to the RC oscillation loops to charge for GNM, where the QDs/ligand system can be treated as a parallel circuit with resistance (R) and capacitance (C). The electron charging time is positive correlating to the time constant τ, where $\tau = RC$. According to capacitance formula $C = \frac{\varepsilon S}{4\pi kd}$, capacitance will be determined by the distance (ligand length) and ε (dielectric constant). Thus, considering the conductivity, ligand length, dielectric constant and lesser defects in pyridine, the response time of GNM/QDs(Py) is shorter compared to that of GNM/QDs(PANI) device.

The responsivity of these devices as well as the response time was calculated under illumination by different wavelengths. Transfer characteristic curves of the GNM/QDs(TOPO) device under some typical wavelengths can be seen in Fig. 5d, which shows a fluctuated decrease from violet to red. The responsivity (R, A W^{-1}) can be calculated from the photocurrent, incident light luminous density and the effective area. The responsivity of different wave estimated by this formula is shown in the inset image of Fig. 5d. As shown in the inset image of Fig. 5d, the responsivity of the GNM/QDs follows the same trend compared with the UV-vis spectrum in Fig. S1c,† where no extra responsivity can be observed outside the absorbance curve. The responsivity also has a relatively higher value near the emission peak wavelength. In addition, the responsivity of the GNM/QDs FET device with other different ligands is shown in Fig. S3d.† The performances of these devices are summarized in Table 1 and compared with other similar graphene/QDs based photodetectors.

Table 1 Device performance comparison of the different devices

Device structure	ligands	Rise time	On/off ration	Resp. (A W^{-1})	Ref.
GNM/QDs FET	TOPO	15 ms	9.1	1800	—
GNM/QDs FET	OA	35 ms	1.15	34	—
GNM/QDs FET	Pyridine	0.64 s	4.2	1760	—
GNM/QDs FET	PANI	>1 s	2.4	574	—
Gra/QDs FET	Pyridine	0.3 s	1.15	2700	10
Gra/QDs FET	Default	~10 s	1.01	8.4 A W^{-1}	31
Gra/QDs FET	Ethane-dithiol	10 ms	~1.5	10^7	37
Gra/QDs vertical-diode	TOPO	0.4 ms	10^4	0.5 A W^{-1}	38
Gra/QDs planar-diode	PANI	~20 s	1.005	Default	19

3. Conclusions

A GNM/QDs hybrid photodetector was developed with high photocurrent on/off ratio to seek effective charge transfer from quantum dots. This work mainly focused on the promotion of the device performance and the mechanism of the effective electron tunnelling. The summary of the devices' performance comparison is concluded in Table 1. The results revealed the following: (1) With the current-limiting effect of the p-type GNM, the photocurrent on/off ratio of the FET-type photodetector can be boosted by nearly one order of magnitude. (2) By utilizing adequate insulating ligands, the higher photocurrent can be obtained due to the effective electron tunnelling from QDs. (Another shorter ethane-dithiol ligand has been used in a graphene/QDs hybrid device in the place of OA ligands, which also showed an excellent performance[37]) (3) Compared with the electroactive ligand, which functions as the electron transport layer, the electron tunnelling across the ligand can curtail the response time toward the high-speed pulse light signal. (4) By the analysis of the tunnelling mechanism, built-in field is a crucial factor for the tunnelling probability, which also influences the response time of the device due to the electron accumulation time in the QDs/ligand interface. We deduced that it is the reason for the longer response time in a planar diode or FET device compared with the vertical-diode device. Obviously, to obtain a higher responsivity of photodetectors, the FET-type photodetector has unique advantages and it is the main aim of our work to find out an effective charge transfer method for the future high-performance graphene-based photodetectors with high speed, responsivity, and high on/off photocurrent ratio.

4. Experimental section

4.1 Formation of GNM

4.1.1 Synthesis of monolayer-graphene. Mono-layer graphene was synthesized by thermal chemical vapor deposition (CVD), which has been reported in detail elsewhere. In brief, 5 sccm CH_4(Air Products, 99.5%) was aerated on to a 50 μm-thick physical vapor deposited Cu foil, at 1000 °C in an Ar : H_2 ballast (960 : 40 sccm) at 350 mbar for 20 min. After quenching in a venting system, the device was cooled down using 2000 sccm N_2.

4.1.2 Electrochemical method to form AAO mask. First, aluminium foil (99.99%) was immersed into a mixture solution ($HClO_4$ (60 wt%)–ETOH = 1 : 4), and then was polished by the Electrolysis method at 20 V. The following is the process for the first anodization. The anode (Al foil) and the cathode (Pt mesh) were placed in a 0.3 M oxalic acid solution at 0 °C. Thereafter, the mixed solution of phosphoric acid (6 wt%) and chromic acid (1.8 wt%) with Al foil was allowed to stand at 75 °C for 10 h to avoid the alumina caused by oxidation. A second anodizing step was then carried out for half an hour in order to form the sequential porous alumina membrane on Al foil, and saturated $HgCl_2$ solution was used on the surface to

exfoliate the AAO membrane. Thereafter, the homologous nanoscale porous AAO with about 40 nm hole and 15 nm ribbon was produced by 5 wt% phosphoric acid for about 1 h. With monolayer CVD-growth graphene transferred to the silica wafer assisted by PMMA film, the AAO membrane was fixed on the surface of graphene as the AAO mask.[39]

4.1.3 GNM FET device fabrication and device lifetime. On the graphene/AAO surface, approximately 5 nm Ti was deposited by RF sputtering method for about 5 s in Ar_2 atmosphere (1.5 Pa) by a Ti target (99.999%) at room temperature. Next, a wet-etching solution (HF and NaOH) was utilized for etching graphene and the AAO mask for about 40 s to form the GNM silica substrate. To define the FET channel, lithography process was used and the Ti (5 nm) and Au (50 nm) electrodes were deposited by thermal evaporation. The as-prepared GNM Si/SiO_2 FET wafer was cut into four pieces for the four devices with different ligands. The four QDs solution samples (about 3 mg mL^{-1}, 50 μL) were released by micropipette toward the FET channels and dispersed using a spin coating process at 1000 rpm to form an approximately 28 nm QDs thin film. Next, a 300 °C annealing process was carried out to bond the QDs and GNM channels. The AFM image in Fig. 2c shows the surface morphology of the QDs film. In the previous section, the significant role of the annealing has been discussed. However, the device, especially the organic ligands bonding GNM and QDs, were exposed to the humid ambient conditions, which could influence the performance of the devices after storage for a period of time.[40] As can be seen in Fig. S4b,† the devices can remain stable for several weeks, but it seems that the device wrapped with pyridine ligands suffers because of the decline of electron transport performance of the pyridine. As we supposed, the TOPO device does not rely on the transport of the organic ligand and as a consequence, this device even showed an excellent performance after storage for three months. Moreover, the thick PANI and OA ligands possibly prevented this device from the oxidation and damp air, and thus it showed a highly stable photocurrent for a long time. Of course, if we could utilize some encapsulation or passivation method for the channel of the device in the future, it will not be very difficult to produce FET-type photodetectors with better stability.

4.2 Synthesis of QDs and GNM/QDs hybrid

4.2.1 Ligand exchange of QDs and ligands storage life time. CdSe QDs (diameter: 4.8 nm) capped with trioctylphosphine oxide (TOPO) and oleic acid (OA) ligands were purchased from Wuhan Jiayuan Quantum Dots CO., LTD, as shown in Fig. S1(a).† The ligand exchange procedure of QDs capped with pyridine (Py) is as follows. QDs(OA) solution was heated (70 °C, 1 h), and then added to ethanol (volume ratio 1 : 2). After centrifuging the mixture, the collected precipitate was pyridine capped with CdSe QDs, which was re-dispersed in toluene by sonication for 2 hours at room temperature. The morphology of the as-prepared QDs (Py) can be seen in the SEM image of Fig. S1(b).† The two steps of synthesizing CdSe (QDs@PANI)[3] are as follows. The first step is to prepare tailored QDs: the TOPO ligands capping on the CdSe QDs are exchanged for 4-formyldithiobenzoic acid ligands, which forms a dithioate bridge between the QDs and the ligand; then, to form the polyaniline encapsulation on the CdSe QDs, the aniline tetramer solution was added to the tailored QDs. After the condensation reaction between the 4-formyldithiobenzoic acid ligands and the tetramer, the aniline tetramer is grafted on the surface of QDs to form the QDs(PANI), as shown in Fig. S1(c).†

4.3 Measurement and instruments

The Morphology of the device microstructure was characterized by scanning electron microscopy (SEM, Hitachi S4800) and the QDs detail image by transmission electron microscopy (TEM, Tecnai G2 F20 U-TWIN). Photoluminescence intensity and time-resolved spectrofluorometer (FL2-21-IHR320-TCSPC) was used to detect the charge transfer in the neutral GNM channel. Keithley 2400 was utilized to characterize the electric properties of the GNM/QDs FET device. High performance Agilent DSO91204A was used to probe the voltage variation in the high speed time trace experiment. LED lamp source with different wavelength diodes and adjustable power was used as the top light-modulated terminal. In addition, the multi-wavelength optic intensitometer DES-100H (U.S.A SP Co. Ltd) was used to confirm the power intensity.

Acknowledgements

This work was supported in part by National Key Basic Research Program 973(2010CB327705), National Natural Science Foundation Project (51120125001, 51350110232, 61372030, 51202028, 91333118 and 51202027), Foundation of Doctoral Program of Ministry of Education (20120092120025), and the Research Fund for International Young Scientists from NSFC (51050110142, 61150110167 and 51150110160).

Notes and references

1 F. Bonaccorso, Z. Sun, T. Hasan and A. C. Ferrari, *Nat. Photonics*, 2010, **4**, 611–621.
2 Q. Bao and K. P. Loh, *ACS Nano*, 2012, **6**, 3677–3694.
3 R.-J. S. Xuetao Gan, Y. Gao, I. Meric, T. F. Heinz, K. Shepard, J. Hone, S. Assefa and D. Englund, *Nat. Photonics*, 2013, **7**, 883–887.
4 S.-H. Cheng, T.-M. Weng, M.-L. Lu, W.-C. Tan, J.-Y. Chen and Y.-F. Chen, *Sci. Rep.*, 2013, 3.
5 S. Heeg, R. Fernandez-Garcia, A. Oikonomou, F. Schedin, R. Narula, S. A. Maier, A. Vijayaraghavan and S. Reich, *Nano Lett.*, 2013, **13**, 301–308.
6 L. G. Cançado, A. Jorio, E. H. M. Ferreira, F. Stavale, C. A. Achete, R. B. Capaz, M. V. O. Moutinho, A. Lombardo, T. S. Kulmala and A. C. Ferrari, *Nano Lett.*, 2011, **11**, 3190–3196.

7 L. G. De Arco, Y. Zhang, C. W. Schlenker, K. Ryu, M. E. Thompson and C. W. Zhou, *ACS Nano*, 2010, **4**, 2865–2873.

8 J. L. S. Jun and E. Jang, *ACS Nano*, 2013, **7**, 6310–6320.

9 M. Zhu, X. Li, Y. Guo, X. Li, P. Sun, X. Zang, K. Wang, M. Zhong, D. Wu and H. Zhu, *Nanoscale*, 2014, **6**, 4909.

10 Z. Sun, Z. Liu, J. Li, G.-A. Tai, S.-P. Lau and F. Yan, *Adv. Mater.*, 2012, **24**, 5878–5883.

11 Z. C. Xiaomu Wang, K. Xu, H. K. Tsang and J.-B. Xu, *Nat. Photonics*, 2013, **7**, 888–891.

12 M. Andreas Pospischil, M. M. Furchi, D. Bachmann, R. Guider, T. Fromherz and T. Mueller, *Nat. Photonics*, 2013, **7**, 892–896.

13 T. J. Echtermeyer, L. Britnell, P. K. Jasnos, A. Lombardo, R. V. Gorbachev, A. N. Grigorenko, A. K. Geim, A. C. Ferrari and K. S. Novoselov, *Nat. Commun.*, 2011, **2**, 458.

14 Y. Liu, R. Cheng, L. Liao, H. Zhou, J. Bai, G. Liu, L. Liu, Y. Huang and X. Duan, *Nat. Commun.*, 2011, **2**, 579.

15 M. Freitag, T. Low, W. Zhu, H. Yan, F. Xia and P. Avouris, *Nat. Commun.*, 2013, 4.

16 S. Kaniyankandy, S. Rawalekar and H. N. Ghosh, *J. Phys. Chem. C*, 2012, **116**, 16271–16275.

17 K. Kim, J. Y. Choi, T. Kim, S. H. Cho and H. J. Chung, *Nature*, 2011, **476**, 338–344.

18 J. Li, L. Niu, Z. Zheng and F. Yan, *Adv. Mater.*, 2014, **26**, 5239–5273.

19 K. T. Nguyen, D. Li, P. Borah, X. Ma, Z. Liu, L. Zhu, G. Grüner, Q. Xiong and Y. Zhao, *ACS Appl. Mater. Interfaces*, 2013, **5**, 8105–8110.

20 J. Bai, X. Zhong, S. Jiang, Y. Huang and X. Duan, *Nat. Nanotechnol.*, 2010, **5**, 190–194.

21 S. Berrada, V. Hung Nguyen, D. Querlioz, J. Saint-Martin, A. Alarcón, C. Chassat, A. Bournel and P. Dollfus, *Appl. Phys. Lett.*, 2013, **103**, 183509.

22 J.-M. Shieh, Y.-F. Lai, W.-X. Ni, H.-C. Kuo, C.-Y. Fang, J. Y. Huang and C.-L. Pan, *Appl. Phys. Lett.*, 2007, **90**, 051105.

23 C. Y. Chien, W. T. Lai, Y. J. Chang, C. C. Wang, M. H. Kuo and P. W. Li, *Nanoscale*, 2014, **6**, 5303.

24 H. Al-Mumen, L. Dong and W. Li, *Appl. Phys. Lett.*, 2013, **103**, 232113.

25 Y. Y. Hui, G. a. Tai, Z. Sun, Z. Xu, N. Wang, F. Yan and S. P. Lau, *Nanoscale*, 2012, **4**, 3118.

26 M. Wang, L. Fu, L. Gan, C. Zhang, M. Rümmeli, A. Bachmatiuk, K. Huang, Y. Fang and Z. Liu, *Sci. Rep.*, 2013, 3.

27 T. Kato and R. Hatakeyama, *Nat. Nanotechnol.*, 2012, **7**, 651–656.

28 Y. Q. Huang, R. J. Zhu, N. Kang, J. Du and H. Q. Xu, *Appl. Phys. Lett.*, 2013, **103**, 143119.

29 X. Geng, L. Niu, Z. Xing, R. Song, G. Liu, M. Sun, G. Cheng, H. Zhong, Z. Liu, Z. Zhang, L. Sun, H. Xu, L. Lu and L. Liu, *Adv. Mater.*, 2010, **22**, 638–642.

30 M. J. Greaney, S. Das, D. H. Webber, S. E. Bradforth and R. L. Brutchey, *ACS Nano*, 2012, **6**, 4222–4230.

31 D. Zhang, L. Gan, Y. Cao, Q. Wang, L. Qi and X. Guo, *Adv. Mater.*, 2012, **24**, 2715–2720.

32 J. de Araújo Gonçalves, A. L. D. Ramos, L. L. L. Rocha, A. K. Domingos, R. S. Monteiro, J. S. Peres, N. C. Furtado, C. A. Taft and D. A. G. Aranda, *J. Phys. Org. Chem.*, 2010, **24**, 54–64.

33 C. Querner, P. Reiss, S. Sadki, M. Zagorska and A. Pron, *Phys. Chem. Chem. Phys.*, 2005, **7**, 3204.

34 B. S. Kim, M. A. Islam, L. E. Brus and I. P. Herman, *J. Appl. Phys.*, 2001, **89**, 8127.

35 H. Zhao, Z. Fan, H. Liang, G. S. Selopal, B. A. Gonfa, L. Jin, A. Soudi, D. Cui, F. Enrichi, M. M. Natile, I. Concina, D. Ma, A. O. Govorov, F. Rosei and A. Vomiero, *Nanoscale*, 2014, **6**, 7004.

36 H. G. Winful, *Phys. Rep.*, 2006, **436**, 1–69.

37 G. Konstantatos, M. Badioli, L. Gaudreau, J. Osmond, M. Bernechea, F. P. G. de Arquer, F. Gatti and F. H. L. Koppens, *Nat. Nanotechnol.*, 2014, **7**, 363–368.

38 K. K. Manga, J. Wang, M. Lin, J. Zhang, M. Nesladek, V. Nalla, W. Ji and K. P. Loh, *Adv. Mater.*, 2012, **24**, 1697–1702.

39 Z. Zeng, X. Huang, Z. Yin, H. Li, Y. Chen, H. Li, Q. Zhang, J. Ma, F. Boey and H. Zhang, *Adv. Mater.*, 2012, **24**, 4138–4142.

40 C. Querner, P. Reiss, J. Bleuse and A. Pron, *J. Am. Chem. Soc.*, 2004, **126**, 11574–11582.